Deformation Monitoring Using Ground-Based Differential SAR Tomography

Huiming Chai, Xiaolei Lv, *Member, IEEE*, and Ping Xiao

Abstract—This letter presents the first differential synthetic aperture radar (SAR) tomography (D-TomoSAR) results using ground-based SAR (GB-SAR) data sets. GB-SAR provides an important deformation monitoring technology for glacier movements, landslides, and infrastructures because of its real-time monitoring capability compared with the airborne and spaceborne SAR sensors. A D-TomoSAR processing framework using region growing is proposed, which does not require the preliminary removal of atmospheric phase screen. The most reliable single-scatterers are identified as seeds, whereas the double-scatterers and unstable single-scatterers are resolved iteratively using region growing. First experimental results on 89 GB-SAR images over the Aletsch glacier, Switzerland, demonstrate the effectiveness of GB D-TomoSAR and the proposed method.

Index Terms—Deformation monitoring, differential tomographic SAR, ground-based (GB), region growing.

I. INTRODUCTION

DIFFERENTIAL synthetic aperture radar (SAR) tomography (D-TomoSAR) [1], [2] allows to profile the scattering distribution on elevation–linear-deformation velocity (s–v) plane. As a result, D-TomoSAR provides a powerful tool for 3-D reconstruction and long-term microdeformation monitoring of urban buildings and infrastructures [3]. Various airborne and spaceborne SAR data sets have been employed to assess the potentials of SAR tomography (TomoSAR) and D-TomoSAR. Compared with the interferometric SAR (InSAR) techniques, such as multibaseline InSAR phase unwrapping based three-pass differential InSAR (DInSAR) [4], persistent scatterer interferometry (PSI) [5], small baseline subsets [6], and joint-scatterer InSAR [7], D-TomoSAR exploits amplitude and phase rather than phase

information only. This concept leads to improved performance in the estimation of location and motion parameters [8]. The superiority of D-TomoSAR, compared to traditional InSAR techniques, lies in: 1) it allows the separation of layover scatterers and 2) it offers higher accuracy in terms of elevation and deformation estimates.

However, the airborne and spaceborne SAR sensors only provide limited long revisit cycles compared with the ground-based SAR (GB-SAR). Consequently, it is difficult to monitor the glacier movements, landslides, and infrastructures in real-time by using airborne and spaceborne D-TomoSAR. Besides, application scenes of spaceborne D-TomoSAR are always limited by the angle of incidence and spatial resolution.

In this letter, we propose the GB D-TomoSAR (GBD-TomoSAR) which provides the capability for real-time monitoring. GBD-TomoSAR is based on the SAR images acquired by GB-SAR. It seems encouraging to directly apply the existing D-TomoSAR techniques to GBD-TomoSAR. However, several considerations need to be taken into account.

The GB-SAR measurements (for deformation mapping scenarios) are usually obtained using a zero-spatial-baseline configuration, i.e., the GB-SAR images are acquired from the same site. As a consequence, GBD-TomoSAR merely estimates the velocity of scatterers and its signal model is definitely different from that of spaceborne D-TomoSAR. Another important issue is that the measurements are often significantly affected by the atmospheric propagation delay. It is necessary to correct the atmospheric phase screen (APS) before differential tomographic processing. Unfortunately, the reliable removal of APS for D-TomoSAR via PSI is a complicated task. A simple yet effective way is, therefore, proposed for D-TomoSAR to correct the APS, which uses short-arc based region growing. By employing the proposed framework, we present the first GBD-TomoSAR results using 89 images over the Aletsch glacier, Switzerland. To establish the effectiveness of the proposed framework and GBD-TomoSAR, we also perform a comparison between the velocity maps retrieved by GBD-TomoSAR and GB PSI.

II. GBD-TomoSAR SIGNAL MODEL

Let $\gamma(s)$ denote the unknown reflectivity distribution along s. Considering N repeat-pass coregistered SAR images, the focused data g_n, $n = 1, 2, \ldots, N$ of a given pixel for the nth acquisition can be expressed as follows:

$$g_n = \int_{\Delta s} \gamma(s) \exp\left(j\frac{4\pi b_n}{\lambda r}s\right) ds \qquad (1)$$

where b_n is the spatial perpendicular baseline, λ is the wavelength, r stands for the slant range between the SAR sensor

and target, and Δs represents the elevation span. Let N_K be the number of scatterers in the pixel and let $d(k, t_n)$ denote the deformation for the kth scatterer at temporal baseline t_n, the spaceborne TomoSAR model (1) can be extended to

$$g_n = \sum_{k=1}^{N_K} \gamma(s_k) \exp\left(j\frac{4\pi b_n}{\lambda r}s_k\right) \exp\left(-j\frac{4\pi}{\lambda}d(k, t_n)\right) \quad (2)$$

where $\gamma(s_k)$ is the reflectivity for the kth scatterer. Spaceborne D-TomoSAR measurements are acquired from slightly different positions, synthesizing an aperture along elevation, and thus, D-TomoSAR provides the imaging ability in elevation. While the GBD-TomoSAR observations are obtained from a fixed place, the spaceborne D-TomoSAR signal model is no longer applicable to the GB case. Substituting zero-spatial-baselines into (2) yields

$$g_n = \sum_{k=1}^{N_K} \gamma_k \exp\left(-j\frac{4\pi}{\lambda}d(k, t_n)\right) \quad (3)$$

where $\gamma(s_k)$ is denoted as γ_k. By expanding the exponential deformation term in Fourier harmonics

$$\exp\left(-j\frac{4\pi}{\lambda}d(k, t_n)\right) = \int_{\Delta v} h(k, v) \exp\left(-j\frac{4\pi t_n}{\lambda}v\right) dv \quad (4)$$

GBD-TomoSAR signal model is formulated as

$$g_n = \int_{\Delta v} \gamma(v) \exp\left(-j\frac{4\pi t_n}{\lambda}v\right) dv, \quad n = 1, 2, \ldots, N \quad (5)$$

where $\gamma(v) = \sum_{k=1}^{N_K} \gamma_k h(k, v)$ is the complex reflectivity profile along v. Although (5) is unable to provide the tomography, it is referred to as GBD-TomoSAR because it contains the extension of TomoSAR notation to the velocity domain and it is still within the context of D-TomoSAR. Discretizing v into $\mathbf{v} = (v_1, v_2, \ldots, v_K)^T$, the GBD-TomoSAR signal model is rewritten as

$$\mathbf{g} = \mathbf{L}\boldsymbol{\gamma} \quad (6)$$

where $\mathbf{g} = (g_1, \ldots, g_N)^T$ is the measurement vector, $\mathbf{L} = (\mathbf{l}(v_1), \ldots, \mathbf{l}(v_K)) \in \mathbb{C}^{N \times K}$ is the steering matrix, and $\boldsymbol{\gamma} \in \mathbb{C}^{K \times 1}$ represents the reflectivity. The GBD-TomoSAR inversion is intrinsically an array signal processing problem, the same as airborne and spaceborne SAR tomography. The spectral estimation (SE) methods can, therefore, be used for GBD-TomoSAR tomographic processing, including beamforming (BF), truncated singular value decomposition [9], Capon filtering, and multiple signal classification. For point-like scatterers in the presence of linear deformation, $\boldsymbol{\gamma}$ is N_K-sparse ($K \gg N_K$) and its different components describe different scatterers. Compressive sensing (CS) can be thus adopted to recover the sparse backscattering $\boldsymbol{\gamma}$ [10], by optimizing the following objective function:

$$\hat{\boldsymbol{\gamma}} = \arg\min_{\boldsymbol{\gamma}} \|\mathbf{g} - \mathbf{L}\boldsymbol{\gamma}\|_2^2 + \tau\|\boldsymbol{\gamma}\|_1 \quad (7)$$

where $\tau \in \mathbb{R}^+$ is a regularization parameter. Model order selection (MOS) [9] is usually executed to detect true scatterers from $\hat{\boldsymbol{\gamma}}$, and the velocity of the scatterers can be retrieved.

GBD-TomoSAR is superior to GB-SAR interferometry (GB-InSAR), which has been developed for deformation measurement [11]. It is expected that GBD-TomoSAR exhibits a
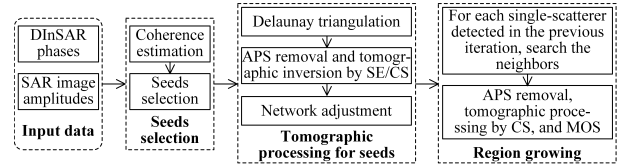
Fig. 1.   Flowchart of the proposed GBD-TomoSAR processing method.

higher parameter estimation accuracy than GB-InSAR because SAR tomography exploits the amplitudes besides interferometric phases [8]. GBD-TomoSAR can be, therefore, used for near-real-time deformation monitoring with high precision. However, the APS is usually removed for D-TomoSAR via PSI in the literature, which is complicated and hinders the application of GBD-TomoSAR. To make the processing of GBD-TomoSAR data easier, we propose a simple and effective strategy that allows the operational processing of GBD-TomoSAR.

III. GBD-TomoSAR Processing Framework

GBD-TomoSAR processing flow mainly includes seeds selection, tomographic processing for seeds, and region growing, as illustrated in Fig. 1. Most stable single-scatterers are identified as seeds, whereas other scatterers are resolved using region growing. In order to improve computational efficiency, our approach is based on permanent scatterer (PS). Note that the region is composed of detected scatterers (spatially discrete PSs). Using the property that APS is slowly variable in space domain [11], the APS of a given seed or PS can be removed by subtracting the phase of a reference point (single-scatterer) that is sufficiently close. Short-arc based region growing is, therefore, adopted to eliminate the APS.

A. Seeds Selection

Most stable PSs are selected as initial seeds (Φ_s) for region growing. Because the seed points will be considered as reference pixels in the region growing, they should be stable single-scatterers. It can be shown that layover and APS always result in low coherence of interferograms [12]. In our framework, the coherence is first computed. Then, the PSs whose average coherence of N interferograms is larger than a predefined threshold C_1 are selected as seeds. C_1 must be sufficiently high to exclude double-scatterers and unstable single-scatterers.

B. Tomographic Processing for Seeds

The parameters of seed points are retrieved and the seeds of instability are cleared. To mitigate the APS, Delaunay triangulation is employed to connect the neighbor seeds. APS is removed for the ending pixel of the arc by subtracting the phase of the starting point. The parameters of arcs are immediately measured by tomographic inversion via spectral analysis or CS estimators. Then, we reject arcs of long distance ($> l_1$) or low stability ($< \gamma_1$). The stability is characterized by

$$\hat{\gamma} = \frac{|\mathbf{l}(\hat{v})^H \mathbf{g}|}{\|\mathbf{l}(\hat{v})\|_2 \|\mathbf{g}\|_2} \quad (8)$$

where $\hat{v}$ is the velocity of the arc, $\mathbf{l}(\cdot)$ is the steering vector, and $\hat{\gamma}$ represents the normalized reflectivity amplitude. Spatial arcs

may also be used in PSI to compensate the APS, and the test in (8) can be performed as well to establish the stability of the arc for PSI by replacing **g** with the phase of **g**. Note that all the selected seeds are regarded to be single-scatterers. After arcs rejection, the triangulation network may be divided into several independent networks. The largest connected component (LCC) should be identified. Once obtaining the parameters for arcs of LCC, we can retrieve the absolute parameters for the nodes of LCC (in correspondence to final seeds Φ_s^0) through network adjustment [13].

C. Region Growing

Tomographic processing of the remaining PSs is iteratively performed in this step. Let Φ_s^t and Φ_d^t represent the single- and double-scatterers detected in the tth ($t \geq 1$) iteration of region growing, respectively, and let Φ_u denote the unprocessed PSs. In the tth ($t \geq 1$) iteration, the neighbors (Φ_n) within a certain distance l_2 are searched from the unprocessed PS set (Φ_u) for each *single-scatterer* detected in the previous iteration, i.e., for each $\phi_s \in \Phi_s^{t-1}$. This single-scatterer is treated as the reference point for the neighbors. After removing APS, the tomographic inversion and MOS are then executed for each neighbor to detect single- and double-scatterers. If the growing criterion is satisfied, then the neighbor is added to the processed region. The growing criterion is defined as follows: the normalized reflectivity amplitude of dominant-scatterer should be greater than a prespecified value of γ_2. The growing process terminates until no points are added to the region in the current stage. The nonlinear motions of the scatterers also lead to multiple components of γ. By using MOS and (8), our framework does not allow the separation of two sources of multiple components of γ which are caused by the layover and nonlinear motions. The detected double-scatterers may, therefore, contain double-components (DCs) induced by nonlinear motions. In this sense, the proposed method and GBD-TomoSAR cannot resolve the response of layover scatterers. Double-scatterers detected by GBD-TomoSAR are denoted as DCs in the following text.

IV. FIRST GBD-TomoSAR RESULTS

In this section, we present the first GBD-TomoSAR results by using a real data set containing 89 GB-SAR images acquired by the Gamma Portable Radar Interferometer-II (GPRI-II) [14] on September 9, 2011, over the Aletsch glacier, Switzerland. GPRI-II is a multi-mode frequency-modulated continuous wave radar with one transmitting and two receiving slotted waveguide antennas, operating at the frequency range of 17.1 to 17.3 GHz. It has a measurement range of about 20 to 10 000 m, a slant range resolution of 0.75 m, and an azimuth resolution of 6.8 m at 1-km range (in the 2-D radar image acquisition mode). The Aletsch glacier, with central coordinates of (N46°26′32″, E8°4′38″), is the largest glacier in the Alps. It is a retreating glacier, covering about 81.7 km^2 in 2011. The GPRI-II data stack was acquired in polar format, as illustrated in Fig. 2, where θ and r are the azimuth scan angle and slant range, respectively. Fig. 3(a) illustrates the radar intensity image with a size of 3932 × 1379 pixels in range × azimuth in the polar coordinates. The extents of θ and r are indicated in Fig. 3(a). The data stack was taken continuously with an interval of 1.5 min. The Rayleigh resolution along the velocity is $\rho_v = (\lambda/2\Delta_T) = 0.079$ m/day, where $\Delta_T = 0.1098$ days is the temporal baseline extent.
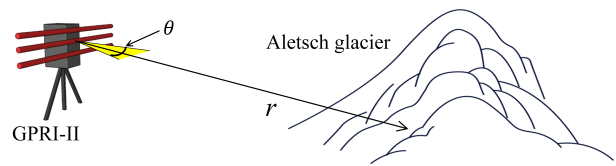
Fig. 2. Geometry of the GB-SAR acquisitions. θ and r are the azimuth scan angle and slant range, respectively.

We first selected the initial seeds for region growing. Fig. 3(b) presents the calculated average coherence of the 89 interferograms. We see that some PSs are with low coherence which may be caused by layover, APS, and temporal decorrelation. To detect the most reliable PSs in the investigated area, the coherence threshold was set to $C_1 = 0.98$, with 437 457 seeds being selected from 821 828 PSs, as shown in Fig. 3(c).

APS correction and tomographic processing were then carried out for the initial seeds. A Delaunay triangulation network was constructed to connect the seed points, as shown in Fig. 4(a). In total, there are 1 311 893 arcs in the triangulated irregular network. Let $\boldsymbol{\varphi}_e \in \mathbb{R}^N$ and $\boldsymbol{\varphi}_s \in \mathbb{R}^N$ denote the differential interferometric phase vector for the ending and starting pixels of the arc, respectively. The phase of the ending pixel after APS calibration is $\boldsymbol{\varphi}_e - \boldsymbol{\varphi}_s$. Tomographic inversion was implemented for the ending seed of each arc. Specifically, BF was utilized without MOS because the seeds are considered to be single-scatterers. The linear velocity is discretized into **v** = $-0.3 : 0.001 : 0.3$ m/day. To achieve a robust parameter estimation of the seeds, arcs with a distance longer than $l_1 = 100$ m or with normalized reflectivity amplitude smaller than $\gamma_1 = 0.9$ were rejected. The number of deleted arcs is 3405, which is relatively small due to the high coherence of interferometric data. Isolated networks may occur as a result of arcs rejection. The LCC of the graph after arc exclusion was distinguished, as shown in Fig. 4(b). By using least-squares, network adjustment computation was then performed for LCC to extract the linear velocity of seeds. Fig. 4(c) depicts the velocity of LCC relative to a reference point (2243, 775). Finally, 436 418 seeds were reserved. It is seen that the glacier shows a significant movement during the observation period. However, only a few pixels were identified in the coverage area of the glacier. The PSs with low coherence are desired to be solved in the region growing step.

In the region growing process, the discrete linear velocity **v** was the same as the one predefined. To enhance the ability of our approach to separate DCs, the CVX toolbox [15] was used to solve (7). MOS was conducted after tomographic inversion for the detection of single-scatterers and DCs. The normalized reflectivity threshold was set to $\gamma_2 = 0.9$. In the first few iterations, l_2 was set to $l_2 = 40$ m, while in the last iterations it was set to $l_2 = 400$ m to reach the isolated PSs. Fig. 5(a) and (d) illustrates the velocity of single-scatterers and DCs with a growing iterate. Compared with the LCC seeds, 293 486 PSs were identified in the first growing iterate, and 20.8% of them were determined to be DCs. It can be seen that the vast majority of PSs with low coherence were resolved using nearby reference points. However, some PSs were not interpolated to the processed region. More iterations were, therefore, required. We also show the final velocity maps in Fig. 5(b) and (e). In total, 740 728 single-scatterers and 66 824 DCs were detected using the proposed method.
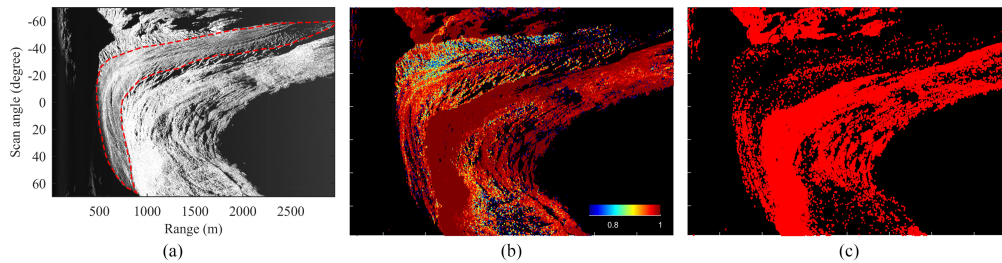
Fig. 3. (a) Average intensity GB-SAR image of the study area in the polar coordinates with the area framed by a red dotted line indicating the Aletsch glacier. (b) Average coherence for all PSs of the 89 interferograms. (c) Selected seeds for region growing.
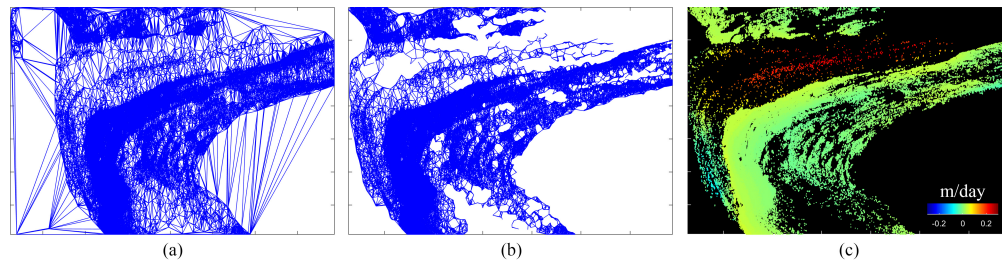
Fig. 4. (a) Delaunay triangulation network. (b) LCC of the graph after arc rejection. (c) Velocity with reference to pixel (2243, 775) for the LCC.
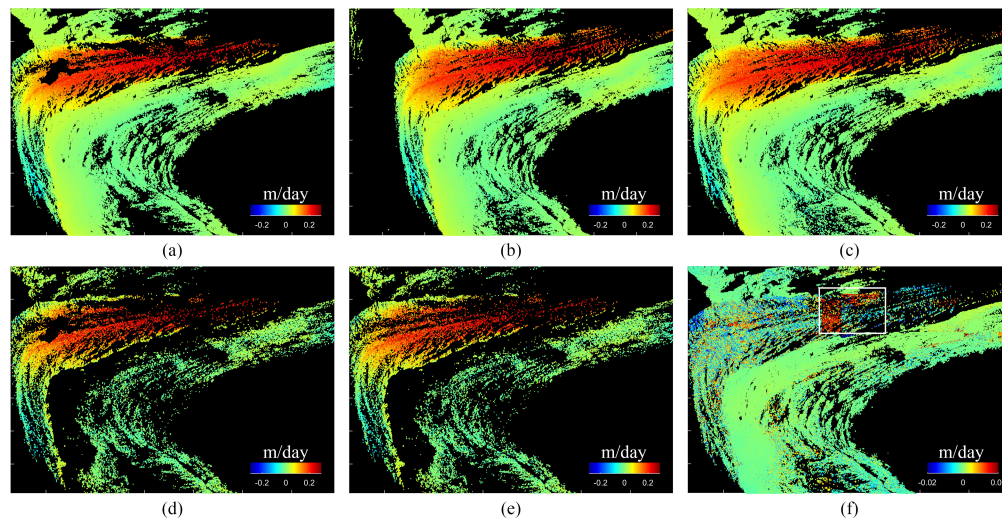
Fig. 5. Linear velocity map retrieved by GBD-TomoSAR for dominant-scatterers (single-scatterers and dominant-components of the DCs) (a) with only one growing iterate and (b) at the end of region growing. (c) Velocity map generated by PSI. (d) and (e) Corresponding velocity of subdominant-components in DCs for (a) and (b). (f) Velocity difference between (b) and (c).

The process stopped after 16 iterations. A more relaxed tolerance l_2 can be utilized to reduce the number of iterations demanded to finish the growing procedure. Yet a too large l_2 leads to APS removing degradation. Large-scale deformation over the glacier is found using GBD-TomoSAR, whereas spaceborne D-TomoSAR may be interfered seriously by the temporal decorrelation owing to the rapid deformation during the long-term observation period and may not be able to deal with glacier movements. GBD-TomoSAR is, therefore, necessary, particularly for real-time and rapid deformation monitoring.

To validate the reliability of our framework, we compare the velocity of dominant-scatterers with the map estimated by GB PSI, as depicted in Fig. 5(c). The reference point of PSI is the same as that of GBD-TomoSAR. The difference between GBD-TomoSAR and PSI solutions

is shown in Fig. 5(f) and the related histogram is shown in Fig. 6(a). We see that the velocity difference of the most scatterers is of small magnitude. The root-mean-square error (RMSE) between two estimates is 0.005 m/day. The small RMSE may be caused by DCs, observed from Fig. 5. There are 93 796 scatterers whose velocity differences are larger than 0.005 m/day with 44 935 PSs being DCs. In other words, compared with GBD-TomoSAR, the velocity for 67.3% of the DCs estimated by PSI is with large bias and the motion parameters achieved by PSI for these PSs may be unreliable. PSI uses the phases only, while GBD-TomoSAR exploits both phases and amplitudes. Thus, it is expected to provide a performance gain over PSI. Moreover, PSI may take the DCs as reference points, which results in incorrect parameter estimation of the PSs using these references, see the rectangle in Fig. 5(f). Fig. 6(b) shows the scatter plot between

This article has been accepted for inclusion in a future issue of this journal. Content is final as presented, with the exception of pagination.

CHAI *et al.*: DEFORMATION MONITORING USING GB DIFFERENTIAL SAR TOMOGRAPHY 5
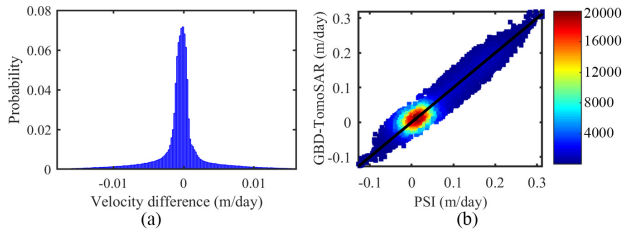
Fig. 6. Comparison between GBD-TomoSAR and PSI. (a) Histogram of velocity differences. (b) Scatter density of velocity estimated by PSI versus GBD-TomoSAR: the color bar is set according to the scatterer density.
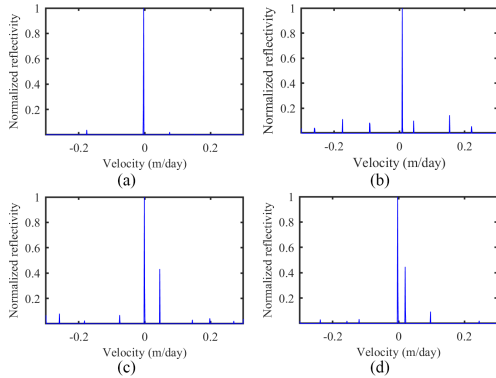
Fig. 7. Reflectivity profiles along linear velocity direction reconstructed by GBD-TomoSAR. (a) and (b) Single-scatterers. (c) and (d) DCs.

the velocity estimated by GBD-TomoSAR and PSI, where the straight black line indicates the optimal fit. The coefficient of determination (R^2) is 0.98, which confirms that the velocity estimated by GBD-TomoSAR has a good consistency with that of PSI.

Reconstructed reflectivity profiles along v are shown in Fig. 7 to further evaluate the validity of the processing chain and GBD-TomoSAR. It is worth noting that the velocity of the reference point had not been added to those of the profiles. Single-scatterers with coordinates of (2047, 966) and (1113, 302) and DCs with (1467, 386) and (1299, 449) were chosen, corresponding to Fig. 7(a)–(d), respectively. From Fig. 7, we find that outliers are very likely to appear in the tomographic imaging. MOS is essential for getting rid of outliers and detecting true scatterers. In our experiments, GB-SAR may suffer from layover in areas that contain highly sloping objects or discontinuous surfaces. The multiple reflections of electromagnetic waves may also contribute to the layover. Due to the illumination geometry of GB-SAR (see Fig. 2), the layover phenomenon is less common in our experiments. There are a few bright pixels produced by layover in the GB-SAR intensity image. Accordingly, the DCs detected are probably induced by nonlinear motions.

V. CONCLUSION

In this letter, we have reported the first experimental results on GBD-TomoSAR and proposed a region growing based

D-TomoSAR processing framework. Experiments on glacier movement verify that GBD-TomoSAR provides the capability of real-time monitoring and tracking the rapid deformation with magnitude up to decimeter/day, and it can be regarded as a complement to airborne and spaceborne differential SAR tomography. Comparisons between GBD-TomoSAR and PSI have also been carried out, where the RMSE and R^2 validate the feasibility of GBD-TomoSAR and processing chain.

REFERENCES

[1] A. Reigber and A. Moreira, "First demonstration of airborne SAR tomography using multibaseline L-band data," *IEEE Trans. Geosci. Remote Sens.*, vol. 38, no. 5, pp. 2142–2152, Sep. 2000.
[2] F. Lombardini, "Differential tomography: A new framework for SAR interferometry," *IEEE Trans. Geosci. Remote Sens.*, vol. 43, no. 1, pp. 37–44, Jan. 2005.
[3] H. M. Chai and X. L. Lv, "SAR tomography for point-like and volumetric scatterers using a regularised iterative adaptive approach," *Remote Sens. Lett.*, vol. 9, no. 11, pp. 1060–1069, 2018.
[4] H. Yu, H. Lee, T. Yuan, and N. Cao, "A novel method for deformation estimation based on multibaseline InSAR phase unwrapping," *IEEE Trans. Geosci. Remote Sens.*, vol. 56, no. 9, pp. 5231–5243, Sep. 2018.
[5] A. Ferretti, C. Prati, and F. Rocca, "Permanent scatterers in SAR interferometry," *IEEE Trans. Geosci. Remote Sens.*, vol. 39, no. 1, pp. 8–20, Jan. 2014.
[6] P. Berardino, G. Fornaro, R. Lanari, and E. Sansosti, "A new algorithm for surface deformation monitoring based on small baseline differential SAR interferograms," *IEEE Trans. Geosci. Remote Sens.*, vol. 40, no. 11, pp. 2375–2383, Nov. 2002.
[7] X. L. Lv, B. Yazici, M. Zeghal, V. Bennett, and T. Abdoun, "Joint-scatterer processing for time-series InSAR," *IEEE Trans. Geosci. Remote Sens.*, vol. 52, no. 11, pp. 7205–7221, Nov. 2014.
[8] G. Fornaro, F. Lombardini, A. Pauciullo, D. Reale, and F. Viviani, "Advanced interferometric and 3-/4-/5-D tomographic processing of SAR data," in *Proc. IGARSS*, Jul. 2016, pp. 1432–1435.
[9] X. X. Zhu and R. Bamler, "Very high resolution spaceborne SAR tomography in urban environment," *IEEE Trans. Geosci. Remote Sens.*, vol. 48, no. 12, pp. 4296–4308, Dec. 2010.
[10] X. X. Zhu and R. Bamler, "Tomographic SAR inversion by L_1-norm regularization—The compressive sensing approach," *IEEE Trans. Geosci. Remote Sens.*, vol. 48, no. 10, pp. 3839–3846, Oct. 2010.
[11] O. Monserrat, M. Crosetto, and G. Luzi, "A review of ground-based SAR interferometry for deformation measurement," *ISPRS J. Photogram. Remote Sens.*, vol. 93, pp. 40–48, Jul. 2014.
[12] W. Xu and I. Cumming, "A region-growing algorithm for InSAR phase unwrapping," *IEEE Trans. Geosci. Remote Sens.*, vol. 37, no. 1, pp. 124–134, Jan. 1999.
[13] G. Liu, S. M. Buckley, X. Ding, Q. Chen, and X. Luo, "Estimating spatiotemporal ground deformation with improved persistent-scatterer radar interferometry," *IEEE Trans. Geosci. Remote Sens.*, vol. 47, no. 9, pp. 3209–3219, Sep. 2009.
[14] C. Werner, T. Strozzi, A. Wiesmann, and U. Wegmüller, "GAMMA's portable radar interferometer," in *Proc. 13th FIG Int. Symp. Deformation Meas. Anal., 4th IAG Symp. Geodesy Geotech. Struct. Eng.*, Lisbon, Portugal, May 2008, pp. 1–10.
[15] M. Grant, S. Boyd, and Y. Ye, *CVX: MATLAB Software For Disciplined Convex Programming*. CVX Res., Inc. Austin, TX, USA, 2008.